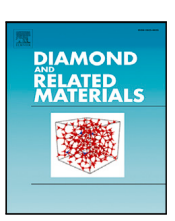
ELSEVIER

Contents lists available at ScienceDirect

# **Diamond & Related Materials**

journal homepage: www.elsevier.com/locate/diamond



# Enhanced boron doping for diamond growth in cylindrical CVD reactors using a Faraday cage

Y. Jiang a b, M. Bose a J.A. Cuenca b, D.L. Creedon a, D. J. Belcourt b, C.D. van Engers d, B. Nadarajah A, K. Ganesan b, J.C. McCallum b, K. Fox b, S. Prawer D.N. Jamieson b, A. Stacey d, D.N. Jamieson b, A. Stacey d, B

- <sup>a</sup> School of Physics, The University of Melbourne, Parkville, 3010, VIC, Australia
- <sup>b</sup> School of Physics and Astronomy, Cardiff University, Cardiff, CF24 3AA, United Kingdom
- <sup>c</sup> CSIRO Manufacturing, Commonwealth Scientific and Industrial Research Organisation, Clayton, 3168, VIC, Australia
- d School of Science, RMIT University, Melbourne, 3001, VIC, Australia
- <sup>e</sup> Quantum Brilliance Pty Ltd, 60 Mills Road, Acton, 2601, ACT, Australia
- <sup>f</sup> School of Engineering, RMIT University, Melbourne, 3001, VIC, Australia
- <sup>8</sup> Princeton Plasma Physics Laboratory, Princeton University, 100 Stellarator Road, Princeton, 08540 NJ, United States of America

#### ARTICLE INFO

# Keywords: Boron doped diamond Superconductivity Chemical vapour deposition FEM simulation Diamond growth

#### ABSTRACT

We report on the use of 3D-printed titanium Faraday cages in a cylindrical resonant cavity CVD reactor for the growth of heavily boron-doped single-crystalline superconducting diamond. We show that the cage enhances boron doping uniformity and provides control of the doping efficiency and growth rate by varying the distance between the plasma and the diamond surface. Using finite element modelling, we demonstrate that the Faraday cage focuses the electric field at the top of the cage whilst also suppressing the electric field inside the cage, thereby pinning the plasma at a fixed height above the sample. This eliminates plasma "hot spots" at the edges of the sample and creates a more uniform plasma electron and hydrogen radical distribution over the sample, resulting in a more uniform boron incorporation.

# 1. Introduction

The possibility of using superconducting boron-doped diamond (BDD) as a superconductor or semiconductor material platform drives the development of synthesis techniques and higher doping methods. Superconducting diamond devices have been demonstrated, such as micro-bridges and wires [1], microwave resonators [2], SQUIDs [3-5], Josephson junctions [6] and mechanical resonators [7]. These devices benefit from sharp interfaces between the intrinsic diamond substrate and the superconducting layer. Boron-doped diamond can be synthesised using the high-temperature-high-pressure (HPHT) method [8] or the chemical vapour deposition (CVD) method [9]. Superconductivity is demonstrated when the boron concentration is above the metalinsulator transition (MIT) threshold of  $n_B \sim 4.5 \times 10^{20} \ {\rm cm}^{-3}$  [10]. The critical temperature  $T_c$  increases with boron doping concentration [11], with reported achievable doping concentration dependent on the crystallographic orientation of the diamond substrate [12]. The onset of superconductivity is reported at temperatures as high as  $T_c \sim 6$  K for homoepitaxially grown BDD on (100) substrates, and up to  $T_c \sim 11~\mathrm{K}$ on (111) substrates [11].

It has been observed that the highest critical temperature can be achieved using a particular geometry of microwave-plasma assisted chemical vapour deposition (MPCVD) reactor [13], which consists of a microwave waveguide pierced by a quartz tube. The sample is inserted into the quartz tube on a sample holding rod and positioned at the intersection of the waveguide and tube where the plasma is ignited. The sample position can be controlled independently of the plasma, whose distribution is determined by the geometry of the waveguide. This type of reactor for diamond growth was first reported by the National Institute for Research in Inorganic Materials (NIRIM) [14], and will be referred to as a "NIRIM-type" reactor in this work. Despite the success with NIRIM-type reactors, most CVD diamond growth is now conducted in scalable resonant cavity reactors, in which the sample holder and plasma position are linked. We have observed that the boron doping uniformity is compromised as the doping concentration increases above the MIT when using such reactors because the plasma 'locks' to the metallic pedestal-type sample stage typically used for growth. This effect is more significant as the boron concentration increases. Furthermore, it is known to be difficult to produce sharp interfaces

E-mail addresses: jiangy1@student.unimelb.edu.au, jiang.yi925@gmail.com (Y. Jiang).

<sup>\*</sup> Corresponding author.

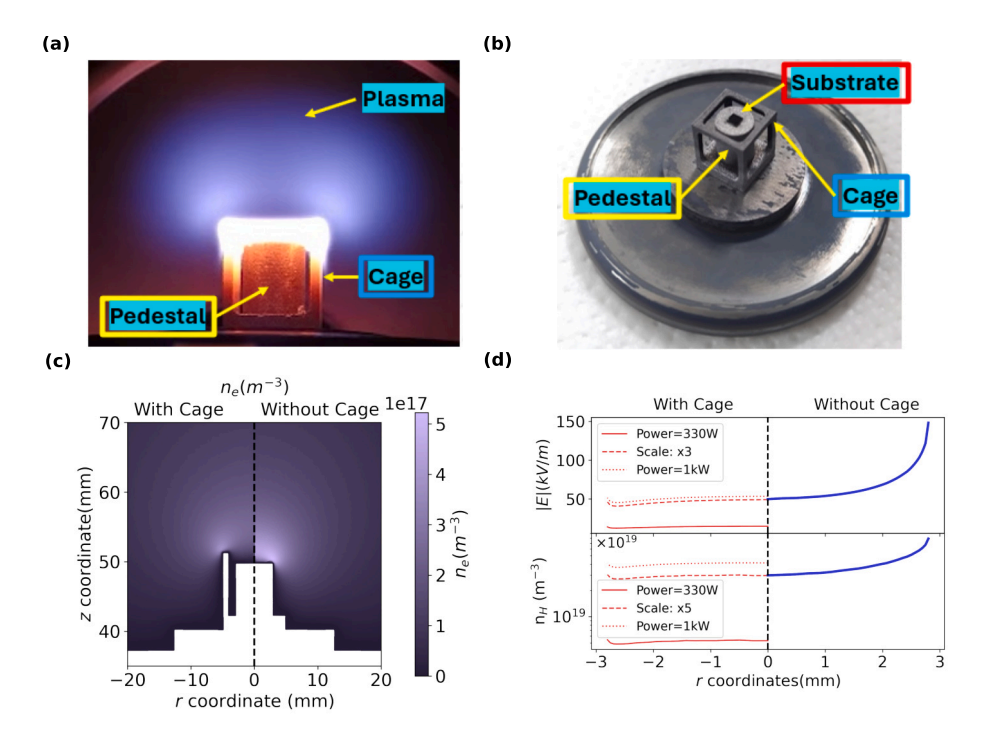


Fig. 1. (a) Cage and plasma during growth; (b) cage layout; (c) electron number density simulation with COMSOL — (left) with the cage and (right) without the cage; (d) comparison of (left) with cage and (right) Hydrogen number density at the pedestal surface using the COMSOL simulation, at d = 1.2 mm. The plasma is focused on the outer structure of the cage instead of the edges of the pedestal, resulting in a more uniform lateral E-field and hydrogen number density distribution across the pedestal. The solid line shows the simulation with actual growth conditions with input power of 330 W; the dashed line shows scale up of |E| and  $n_H$ , indicating plasma intensity reduced by factor of 3 for |E| and 5 for  $n_H$  due to the precense of the cage; the dotted line shows simulation results with input power of 1000 W.

under high-pressure growth conditions where the active species have long residence times, motivating the search for superconducting layers grown at lower pressures.

Metallic intra-cavity structures have been used previously to modify the distribution of the microwave plasma in resonant cavity reactors. The use of a Faraday cage in a clamshell CVD reactor [15] was shown to allow higher uniformity of diamond coatings on 3D objects [16, 17], and the use of a recess-type sample holder has been used to reduce the growth of polycrystalline diamond near the edges of the substrate [18,19]. The recess holders may change the relative position of the plasma and diamond surface, by making an indent in the middle of the holder for the substrate to sit under the sample holder surface; it has been observed that diamond growth is suppressed in a recess holder within a millimetre from the top of the sample holder [20]. The effects of the relative position of the plasma and diamond surface on the crystalline quality of diamond grown in NIRIM-type reactors has been studied [21]; and critically for boron doping above the MIT, it has been shown that such effects can result in dramatic improvements to boron incorporation efficiency [22] when the sample-to-plasma distance is varied by up to 10 mm.

In this work, we introduce the use of a Faraday cage to enable the controlled separation of the plasma from the sample surface. We study the effects of the cage both experimentally and through finite element modelling (FEM) as shown schematically in Fig. 1. We find that the Faraday cage displaces the plasma away from the sample and enhances doping uniformity. We experimentally achieve a high doping concentration of  $n_B \sim 10^{21}~{\rm cm}^{-3}$  in a cylindrical metallic CVD reactor. We also investigate the effect of different sample-to-plasma distances on the boron doping concentration and growth rates by changing the height of the sample holding pedestal within the Faraday cage. Compared to a recess holder, the 3D cage does not appear to suppress growth and doping significantly when the sample surface is 1.2 mm below the top surface of the cage. Using this method, we demonstrate

the growth of (100) diamond layers with critical temperatures above 1 K and uniform doping, suitable for the construction and investigation of superconducting circuit devices.

# 2. Experimental methods

#### 2.1. Diamond growth and device fabrication

The Faraday cages were 3D–printed using Grade 5 Titanium (Ti–6Al–4V) powder with 6% Al and 4% V with a particle size of approximately 25–45  $\mu m$  (ELI; TLS Technik GmbH & Co., Bitterfeld–Wolfen, Germany) using a SLM250HL machine (SLM Solutions, Germany). Cages were printed at laser power of 100 W, scanning speed 375 mm/s and layer thickness 30  $\mu m$  using the method detailed by Xu et al. [23]. The cages were cleaned with isopropanol (IPA) and deionised (DI) water, and blow dried with nitrogen before use. The cages were coated with polycrystalline diamond before growth for 30 min using the same recipe as the sample growth to avoid metallic contamination from the cage being deposited onto the sample surface. The outer cubic frame of the cage has dimensions of width  $\times$  length  $\times$  height = 10 mm  $\times$  10 mm  $\times$  11 mm.

To minimise the effect of substrate miscut angles on doping efficiency [12], the (100)-oriented 4 mm×4 mm single-crystalline diamond substrates (Ra < 2 nm) (EDP Corporation, Osaka, Japan) were laser cut into four pieces. This provides 4-piece sets of identical miscut angles substrates, enumerated by the original seed number. They were cleaned with acid boiling, with 0.25 g sodium nitrate (NaNO<sub>3</sub>) and 3 mL concentrated 98% sulphuric acid ( $H_2SO_4$ ) at  $\sim 550~^{\circ}C$  to remove the graphitic compounds from laser cutting, cleaned via sonication sequentially in acetone, IPA, and DI water, and nitrogen blow dried before growth. Epitaxial growths by Microwave Plasma Enhanced Chemical Vapour Deposition (MPCVD) were then performed in a Seki Diamond Systems ASTeX 6300 reactor with an RF heater stage and maximum power of

1.5 kW. Prior to the introduction of the gases, the stage is heated under vacuum to drive out residual gases and avoid embrittlement of the cage. The growth was carried out for 8 min with a microwave power of 330 W, chamber pressure of 30 Torr, and susceptor plate heating around 500 °C in a gas mixture of CH $_4$ , H $_2$  and trimethylborane (TMB) diluted in H $_2$  (3.7% CH $_4$  in H $_2$ , B/C ratio 34,500 ppm). Fig. 1(a) and (b) show a side view photo of the plasma distribution around the cage during growth, and a view of the configuration of the substrate and cage after growth.

To study the confounding effect of separation between the plasma and the sample surface, the Faraday cages are designed with a pedestal inside the cage to raise the sample. Pedestals with different heights allowed for variation of the distance from the plasma to the sample surface. We define the distance between the sample surface and the top of the cage to be d, as shown in Fig. 3(f). Growths were conducted by varying d while keeping all other growth parameters constant. There are no obvious visible differences in the plasma when varying d. Measuring the sample temperature is difficult inside the cage; however, the sample temperature appears to be similar from the infrared camera.

Hall bars were fabricated for electrical measurements of the epitaxially grown boron-doped diamond layers. Before the lithographic fabrication process, the post-growth samples were sequentially cleaned with acetone, IPA, and DI water in an ultrasonic bath for 5 min and blow dried with nitrogen. A 150 nm aluminium metal mask was evaporated onto the diamond substrate with a Thermionics electron beam evaporator as a shadow mask and image reversal photoresist (AZ 5214E-IR) was deposited via spin-coating. An Oxford Instruments PlasmaLab 100 ICP380 system was used for reactive ion etching with an  $Ar/O_2$  inductively coupled plasma (ICP). The samples were then acid boiled with the same recipe as above to remove the metal mask, and sequentially cleaned in an ultrasonic bath with acetone, IPA, and DI water for 5 min and blow dried with nitrogen. Metal contact pads (Ti/Pt/Au with thickness of 20 nm/10 nm/120 nm respectively) were then deposited onto the device using the same lithography process described above.

#### 2.2. Sample characterisation

To measure the thickness of the MPCVD epitaxial BDD layers, a small diamond flake is placed in the corner of the diamond substrate before growth. This acts as a mask that can be removed post-growth, allowing the epitaxial layer thickness to be determined by measuring the step height with a Bruker Contour GIT-I optical profilometer system. Raman spectra were obtained using a Renishaw inVia Qontor system with 532nm laser, with accumulation time 200 s, diffraction gratings 1800 l/mm, and a 100× objective lens. Time-of-Flight Secondary Ion Mass Spectrometry (ToF-SIMS) measurements were recorded on an ION-TOF ToF-SIMS 5. Depth profiling is performed by exposing an area of the sample to alternating ion beams for sputtering and analysis. A  $100 \times 100 \ \mu m^2$  area was sputtered using 2 keV Cs+. The primary (analysis) beam was 30 keV Bi+ over  $24\times24 \mu m^2$  aligned with the centre of the sputter crater. The boron concentration was calibrated using a diamond sample implanted with a known dose of boron for reference. The mass resolution was  $M/dM \ge 8000$ .

Transport measurements for isolated Hall devices were conducted in a dry dilution refrigerator (Leiden Cryogenics, Netherlands). The electronics for such measurements include a lock-in amplifier, a Source-Measure Unit and a precision nanovoltmeter with a filtering preamplifier.

# 3. Modelling

To understand the primary effect of the Faraday cage on the plasma properties, finite element modelling with COMSOL Multiphysics was employed. The model utilises the Radio Frequency module, Plasma module, and Heat Transfer module.

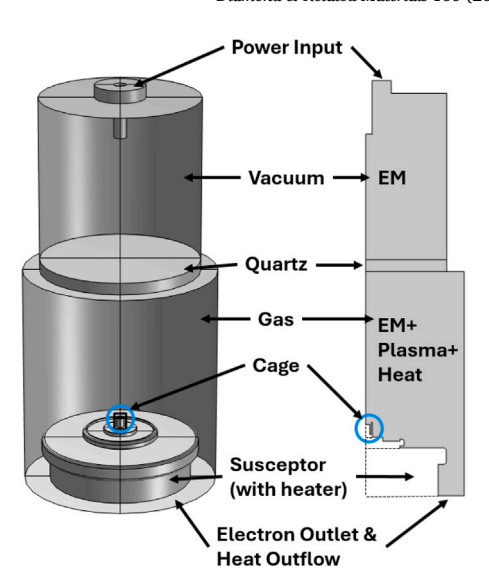


**Fig. 2.** *left*: 3D illustration of the CVD reactor and the cage. *right*: Boundary conditions and computation regions. *Note that* we modelled with the geometry with a cylindrical symmetry, the revolution around the *z*-axis will result in the cage geometry looking like a tall empty cylinder surrounding a pedestal-type sample holder, so that the cage in this simulation will work more like a recess-type sample holder.

In a similar manner to Silva et al. [24], we used 2D axisymmetric geometry to save computational resources as shown on the right-hand side of Fig. 2. Because of this choice of geometry, the cage is actually modelled as a cylinder surrounding the pedestal. Note that this does not make the simulation a physical representation of the actual geometry of the cage, which is a cube. This computational simplification limits the model in two significant ways: it does not include the effect of sharp cage edges and corners, and it does not represent the highly porous walls of a cage. The effect of the choice for the cage geometry will be discussed in Section 5.2. We modelled the geometry of the reaction chamber and used the boundary conditions as shown in Fig. 2. The lower part of the model consists of a graphite susceptor stage that supports the sample holder in the main reaction chamber where the plasma is ignited. The upper chamber consists of a symmetric plasma coupler that converts the TE mode into the  $TM_{013}$  mode. There is a quartz window to define a lower gas region that is transparent to microwave radiation.

# 3.1. Electromagnetic field module

The basic working principle of an MPCVD reactor uses a microwave cavity resonator within which an electromagnetic standing wave is formed. At the electric (E) field anti-nodes, the plasma is formed where the diamond substrate is positioned. Initially the geometry of the plasma is determined by the electric field distribution in the cavity, suggesting that a simple EM model could give a quick proof-of-principle result. With the addition of the Faraday cage, the E-field is perturbed, which results in a shift of the eigenfrequency of the resonance cavity downward. The E-field focuses towards the top of the cage, such that the highest microwave power density will induce a plasma at the top of the cage.

The EM field inside the reactor can be obtained by solving Maxwell's equations

$$\nabla \times \left( \frac{\nabla \times \vec{E}}{\mu_r} \right) - k_0^2 \left( \varepsilon_r - \frac{i\sigma}{\omega \varepsilon_0} \right) \vec{E} = 0 \tag{1}$$

where  $k_0^2 = \omega^2 \epsilon_0 \mu_0$ , and  $\omega = 2\pi f$  is the angular frequency of the EM

We employ the following boundary conditions:

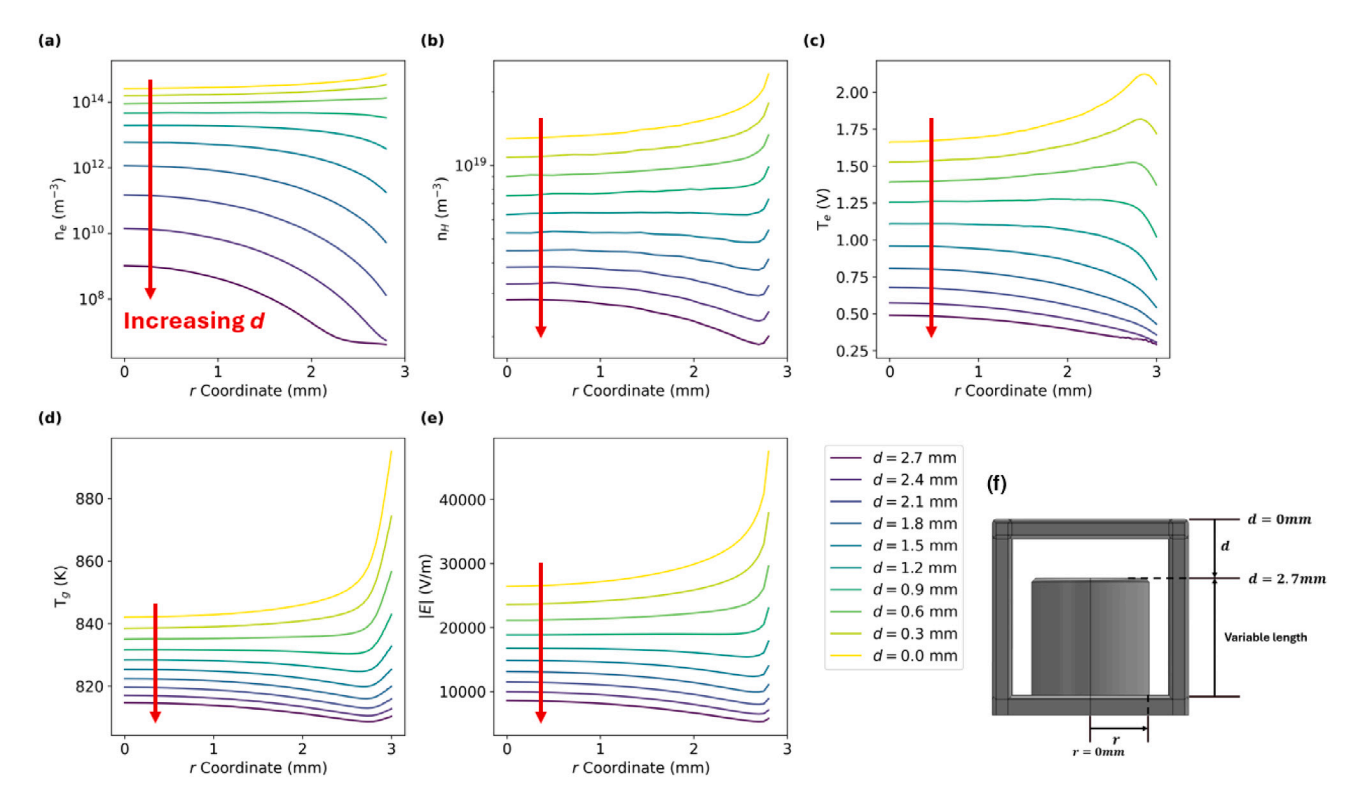


Fig. 3. (a) Electron number density  $n_e$ , (b) H radical number density  $n_H$ , (c) electron temperature  $T_e$ , (d) gas temperature  $T_g$  and (e) E-field with respect to d. The magnitude of these parameters decreases with d increases, as the pedestal is further away from the high intense region of the plasma, with increasing uniformity in r-coordinates for  $T_e$  and |E|. The red arrows in the figures point in the direction of increasing d.

- 1. Perfect electric conductor (PEC) for the reactor side walls, susceptor stage, pucks and pedestal, and the Faraday cage with the following equation:  $\vec{n} \times \vec{E} = 0$ .
- 2. A coaxial microwave port at 2.45 GHz with input power of 330 W at the top of the chamber for EM excitation.

The electric field distribution at the eigenfrequency of the CVD reactor is simulated at the surface of the pedestal with respect to the coordinate r, where r=0 mm is at the centre of the pedestal and  $r=\pm 2.8$  mm is at the edge of the pedestal. The upper part of Fig. 1(d) shows the electric field distribution with and without a Faraday cage at near 2.45 GHz. In the case without the cage, the E-field is around  $\sim 50$  kV/m at r=0 mm. When the cage is present, the E-field inside the cage is suppressed to  $\sim 15$  kV/m, which is still significantly higher than the breakdown field of 9 kV/m at 30 Torr in a reactor with the same geometry [25,26], which suggests that the plasma is not completely excluded from the inside of the cage. The cage provides a sharp structure above the pedestal for the E-field to focus on, so that the E-field does not cling to the edges of the pedestal, leading to a less significant local enhancement at the pedestal.

Moreover, as shown in Fig. 1(d), the enhancement of the E-field near the edge of the pedestal at  $r\approx 2.8$  mm is different with and without the presence of the cage. When the cage is absent, the E-field increases to  $\sim 150$  kV/m around the edge of the pedestal, which is an order of magnitude higher than the E-field near the centre. This is caused by local enhancement in the E-field due to the sharp edges of the pedestal. When the cage is present, the E-field near the edges shows  $\sim 6\%$  change to the centre.

Since the cage holds the most intense part of the plasma away from the pedestal and sample, the height of the pedestal is expected to set the plasma-to-sample distance. As mentioned in Section 2.1, we define the distance from the top of the sample to the top of the cage as d, and henceforth we use this as a proxy for the plasma-to-sample distance. When the distance d=0.0 mm, the sample surface is at the same

level as the top of the cage; as the sample surface goes deeper into the cage, d increases. Fig. 3(e) shows the modelled change in E-field intensity with respect to d. It can be observed that as d increases, the E-field is increasingly suppressed in magnitude, but is still above the breakdown field limit to generate a weak plasma even for d=2.7 mm. Furthermore, as d increases, the enhancement of the E-field near the pedestal edges becomes less pronounced. The edge enhancement effect is the most significant as d decreases to d=0.0 mm, when the E-field is concentrated onto both the pedestal edge and the outer frame of the cage. For d values ranging from 0.9 mm to 2.7 mm, the edge enhancement is suppressed, resulting in a substantially improved E-field uniformity across the surface of the pedestal.

#### 3.2. Plasma module

The EM distribution can be used to predict the basic distribution of the plasma; it does not take into account the effects of chamber pressure or the effects of the ionised gas. These plasma parameters are primarily dominated by hydrogen in diamond growth plasmas. It is known that the H number density determines growth rate, and the distribution of CH<sub>3</sub> follows from H [27], and this allows us to do a hydrogen plasma modelling for the study to understand the plasma and predict the growth rate. Therefore, we will simulate hydrogen-only plasmas. After calculating the electric field distribution, we use a Plasma Module to solve for: the conductivity and permittivity of the plasma, electron number density, Hydrogen number density, and electron temperature. These parameters were then transferred into the heat transfer module, described in the next section, to calculate the gas temperature. The gas temperature will then be updated in the plasma module, and updated in the EM module along with the contribution from the plasma module.

In this work, we include the addition of a simplified H<sub>2</sub> plasma. The conductivity and permittivity of the plasma is given by

$$\begin{split} \sigma_P &= \frac{\omega_P^2 \epsilon_0 v_m}{\omega^2 + v_m^2} \\ \epsilon_P &= 1 - \frac{\omega_P^2}{\omega^2 + v_m^2} \end{split} \tag{2}$$

where  $\omega_P = \sqrt{\frac{e^2 n_e}{\epsilon_0 m}}$  is the plasma frequency, where  $n_e$  is the electron number density  $v_m$  is the collision frequency between electrons and other species, e and  $m_e$  are electron charge and mass.

The electron density and electron energy density can be obtained by solving the drift–diffusion equations where the first equation describes the rate of change of electron density  $n_e$ , and the second equation describes energy conservation:

$$\frac{\partial}{\partial t} (n_e) + \nabla \cdot \left[ -n_e \left( \mu_e \cdot \vec{E} - \nabla \left( \vec{D}_e n_e \right) \right) \right] = R_e$$

$$\frac{\partial}{\partial t} (n_{\varepsilon}) + \nabla \cdot \left[ -n_{\varepsilon} \left( \mu_{\varepsilon} \cdot \vec{E} - \nabla \left( \vec{D}_{\varepsilon} n_{\varepsilon} \right) \right) \right] + \vec{E} \cdot \Gamma_e = R_{\varepsilon}$$
(3)

where  $\mu_e$  is the electron mobility,  $\vec{D}_e = \mu_e T_e$  is the electron diffusivity,  $R_e$  is the electron source;  $n_\epsilon$  is the electron energy density,  $\mu_\epsilon = (5/3)\,\mu_e$  is the energy mobility,  $\vec{D}_\epsilon = \mu_\epsilon T_e$  is the energy diffusivity,  $\Gamma_e$  is the electron flux vector, and  $R_\epsilon$  is the energy loss due to inelastic collisions.  $R_e$  and  $R_\epsilon$  are given by the following:

$$R_{e} = \sum_{j=1}^{M} x_{j} k_{j} N_{n} n_{e}$$

$$R_{\varepsilon} = \sum_{j=1}^{P} x_{j} k_{j} N_{n} n_{e} \Delta \varepsilon_{j}$$

$$(4)$$

where P and M denote the number of inelastic electron-neutral collisions and the electron density source or sink reactions respectively. For the jth reaction,  $x_j$  and  $k_j$  are then the mole fraction of the species and rate coefficient respectively;  $N_n$  is the number density of neutral particles, and  $\varepsilon_j$  is the energy loss from the jth reaction.

The rate coefficients are calculated by

$$k_{k} = \gamma \int_{0}^{\infty} \varepsilon \sigma_{k}(\varepsilon) f(\varepsilon) d\varepsilon \tag{5}$$

where  $\gamma = \sqrt{2e/m_e}$ ,  $\sigma_k$  is the collision cross section given by the chosen reactions which will be discussed later, f is assumed to be Maxwellian electron energy distribution function (EEDF).

The electron temperature is given by

$$T_e = \frac{2}{3}\bar{\epsilon} \tag{6}$$

where  $\bar{\varepsilon} = n_{\varepsilon}/n_{\varrho}$  is the mean electron energy.

For heavy species, we solve the Maxwell–Stefan equations with the mixture-average diffusion model to save computation resources:

$$\rho \frac{\partial}{\partial t} w_k = \nabla \cdot \vec{j}_k + R_k \tag{7}$$

where for the kth species,  $w_k$  is the mass fraction for the species,  $\vec{j}_k = \rho w_k m \vec{V}_d$  is the diffusive flux vector and  $R_k$  is the rate expression, and  $\vec{V}_d$  is the diffusion velocity.

The simplified chemical reaction set follows the work of Cuenca et al. [28], and is listed in Table 1. Electron- $H_2$  elastic collisions, excitations, ionisation and dissociation are included, such that the reactions that describe energy transfer during collisions are considered, and excluding the reactions that have relatively lower rate coefficients or low concentration [29,30]. The heavy-species to heavy-species collisions are ignored in this case, as we are using relatively low microwave power input during the growth, so that these reactions are relatively weak [31]. The cross-section collision data are retrieved from the LxCat (retrieved 11/05/2024) database.

To allow the excited species to be neutralised at the wall, the following surface reactions are implemented [28]:

**Table 1** H<sub>2</sub> reactions used in the plasma module.

Reaction	Formula	Туре	$\Delta \varepsilon  (\mathrm{eV})$
1	$e + H_2 \rightarrow e + H_2$	Elastic	$m_r = 2.74 \times 10^{-4}$
2	$e + H_2 \rightarrow e + H_2(r)$	Rotational excitation	0.044
3	$e + H_2 \rightarrow e + H_2(v)$	Vibrational excitation	0.516
4	$e + H_2 \rightarrow e + 2H$	Dissociation	8.9
5	$e + H_2 \rightarrow e + H_2 *$	Excitation	8.9
6	$e + \mathrm{H_2} \rightarrow 2e + \mathrm{H_2} +$	Ionisation	15.4

- 1.  $H \to 0.5H_2$
- 2.  $H_2 + \rightarrow H_2$
- 3.  $H_2 * \rightarrow H_2$

The following boundary conditions are implemented:

- 1. An electron outlet for the background gas, such that  $-\vec{n}\cdot\Gamma_e=0$  and  $-\vec{n}\cdot\Gamma_e=0$ .
- 2. Wall and ground for the outer walls of the main reaction chamber, where the potential V=0, so that the electron number density is zero at these boundaries.

Note that the EM module needs to be calculated before any plasma module calculation. With the implementation of a sample holder, the eigenfrequency of the reaction chamber will slightly shift away from 2.45 GHz [28], although experimentally the magnetron provides a broad range of frequencies about 2.45 GHz. It is assumed that the magnetron is capable of exciting the correct eigenfrequency as determined by the EM module.

#### 3.3. Heat transfer module

The heat transfer model is implemented to calculate the gas temperature distribution by solving the continuity equations

$$\rho C_P \frac{\partial T}{\partial t} + \nabla \cdot \vec{q} = Q$$

$$\vec{q} = -k \nabla T$$
(8)

where  $\rho$  and T are the density and temperature of the gas,  $C_P$  is the heat capacity, k is the thermal conductivity and Q is the heat source from the electron-neutral gas molecule collisions.

The following boundary conditions are implemented for the heat transfer module:

- Constant temperature of 800 K at the sample holding stage, assuming perfect thermal conductivity between the pedestal and the cage.
- Heat flux at the outer stainless wall and the quartz window, with convective heat flux and heat transfer coefficient being 1700 W/m<sup>2</sup>K, assuming perfect water cooling. This value varies depending on the reactor configuration.
- A heat outflow at the electron outlet, which is an outlet for the background gas.

The simulation uses the three modules to calculate the plasma inside the CVD reactor.

Figs. 1(c) and (d) show a comparison of the electron and hydrogen number densities with and without the cage. In Fig. 1(c), one can clearly observe the dislocation of the plasma away from the pedestal by the Faraday cage. The most intense region does not occur near the surface, like in the case without the cage; instead, it occurs at the top of the outer structure, which is the tall vertical cylinder surrounding the pedestal. It effectively suppresses the electron number density and the E-field inside. As shown in Fig. 1(d), at the centre of the pedestal r=0 mm, the Hydrogen number density  $n_H$  is calculated to be  $5\times 10^{18}$  m<sup>-3</sup> at the surface of the pedestal with the cage, whereas in the case without the cage,  $n_{H^{\sim}} 2\times 10^{19}$  m<sup>-3</sup>. The suppression of E-field

edge enhancement is also seen to result in a more uniform distribution of atomic hydrogen in the case with the cage. Near the pedestal edge, in the case with the cage, there is only a  $\sim 2\%$  change in  $n_H$  from centre to edge; without the cage, there percentage difference is  $\sim 60\%$  from centre to edge. We show on the left-hand side of Fig. 1(d) a 3× dashed line of the solid line as a guide to the eye.

The effect of power is also shown in Fig. 1(d) as a dotted line. If the simulation is performed with approximately 3× the input power of 330 W, the same apparent plasma uniformity can be retained, while the simulated E-field and atomic hydrogen densities can be increased. Boron incorporation is known to increase with increasing power under some process regimes and is expected to be minimally sensitive to power under higher power and pressure regimes. However, our experimental configuration did not allow for controlled sample temperatures at such high powers, limiting the scope of this study.

A study of the distance from the cage top to the pedestal surface d was also performed, shown in Fig. 3. As discussed in Section 3.1, the E-field at the pedestal surface increases as d decreases, while the edge enhancement is conversely suppressed as the pedestal goes deeper inside the cage. This trend is the same for H number density  $n_H$ , electron temperature  $T_e$  and gas temperature  $T_g$ . The electron number density  $n_e$  is more uniform in the r-coordinate when d is small, and its amplitude decreases as d increases.

With higher E-field intensity for decreased d, it can be observed that  $T_e$  increases from  $0.5~{\rm eV}$  to  $1.7~{\rm eV}$ . High  $T_e$  and  $n_e$  result in an increasing number of collisions with heavy species. This is consistent with literature reports of growth rates decreasing as the sample is deep within recess holders. This in turn results in a higher temperature at the pedestal surface, increasing from  $815~{\rm K}$  to  $840~{\rm K}$ , as shown in Fig. 3(d).

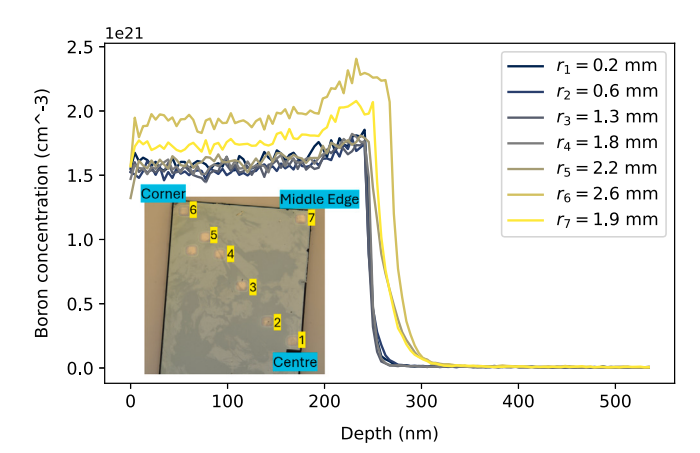
Near the edges of the pedestal, similar observations can be made. The sharp edges of the pedestal enhance the electric field intensity, resulting in higher gas temperature and H number density in the region. As d increases, the electron temperature decreases with the intensity of the E-field as expected. The gas temperature near the edge changes more dramatically as d approaches zero. As the gas temperature increases with the E-field near the edges, there is a dip in the electron temperature. This is consistent with an enhanced energy transfer between electrons and gas temperature.

#### 4. Experimental results

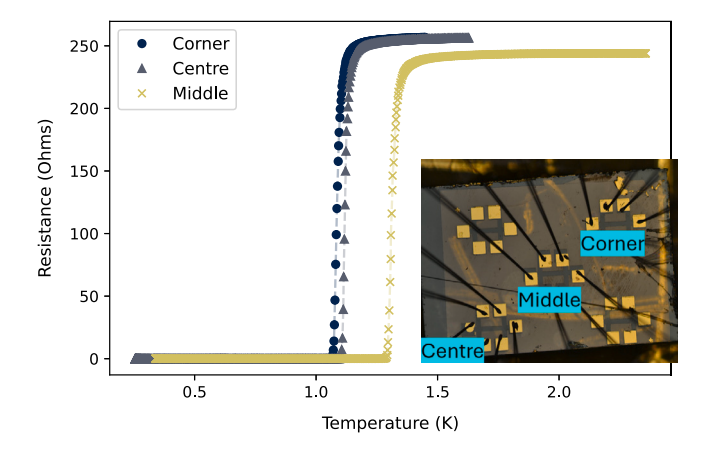
Fig. 1(a) shows a photograph of the typical microwave plasma with the Faraday cage during growth, approximately 3 min after plasma ignition. The shape of the plasma resembles that of the simulation results. Notice that in the photograph and the simulation, the plasma looks highly non-uniform, with enhanced plasma emission at the corners of the top of the outer structure of the cage and decreased electron density in between the two intense regions. From the simulation, we expect a more uniform  $n_e$  at the surface of the sample.

To study the effect of employing a Faraday cage on boron doping, we performed the experiments as described in Section 2 with different d.

To measure the uniformity of boron-doping across the sample, Secondary Ion Mass Spectrometry (SIMS) was performed on a sample grown using d=1.2 mm at different spatial points across the sample, from the centre of the sample to the corner of the sample with the positions labelled as crater number 1–6. An additional edge point at the middle of the sample edge labelled crater number 7 was also performed, as shown in the inset of Fig. 4. These data reveal that the sample has a mostly uniform boron concentration across the centre, from craters 1 to 5, and only a slight increase in boron concentration near the edges (crater 7) and corners (crater 6) of the sample. Near the centre of the sample, the boron concentration is approximately  $1.5 \times 10^{21}$  cm  $^{-3}$ . This boron concentration is above the metal–insulator transition of  $\sim 4.5 \times 10^{20}$  cm  $^{-3}$  [10]. At such a high doping level, the wave functions of the acceptors overlap [32], causing the impurity band and valence



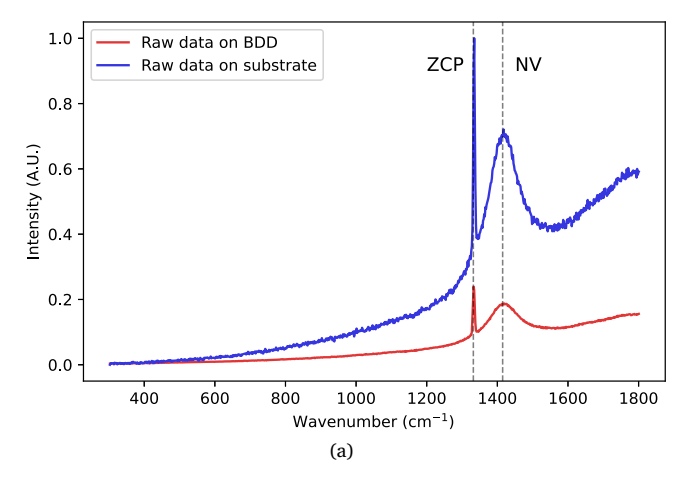
**Fig. 4.** SIMS measurement of boron, with the distance between the centre of the sample (r=0 mm) and the point being measured labelled. The boron concentration is mostly uniform across the sample, and slightly higher near the corners and edges. The sample is originally a  $4 \text{ mm} \times 4 \text{ mm}$  sample and was cut in half. The "Middle Edge" label in the inset figure refers to the middle of the edge of the original sample. The sample is grown with d=1.2 mm.



**Fig. 5.** Transition temperature measurement of three Hall bars on the sample grown at  $d=1.2\,$  mm. The  $T_c$  is 1.1 K for "centre" and "middle" Hall bars, and 1.3 K for the "corner" Hall bar. The slightly higher  $T_c$  for the "corner" Hall bar agrees with the slightly higher boron concentration in that region. Notice that the original sample was cut into four pieces; the inset figure shows a quadrant of the original sample. "Centre" and "corner" in the label refer to the centre and corner of the original sample, "middle" refers to the middle area between the corner and the centre of the original sample.

band to merge, resulting in metallic conduction in this sample. Further SIMS was also performed to show no measurable Ti signatures within the bulk of the boron-doped growth layer. However, there was no Ti-in-diamond reference sample available to determine the minimum detectable limit; therefore, we cannot provide a calibrated sensitivity threshold.

Cryogenic critical temperature measurements were taken inside a dilution refrigerator, as shown in Fig. 5. Three Hall bars were fabricated across the surface of a sample grown at d=1.2 mm, which span the centre, middle, and corner of the sample to further study the uniformity of the boron doping. While the centre and middle Hall bars show similar normal state resistance of  $\sim 250~\Omega$  and critical transition temperature of 1.1 K, the corner Hall bar shows a higher transition temperature of 1.3 K, and slightly lower normal state resistance. Substitutional boron contributes to the density of acceptor states at the Fermi level, which increases  $T_c$  [33]. Our results agree with previous comparisons between boron concentration and  $T_c$ , namely that  $T_c$  increases as boron concentration increases [11].



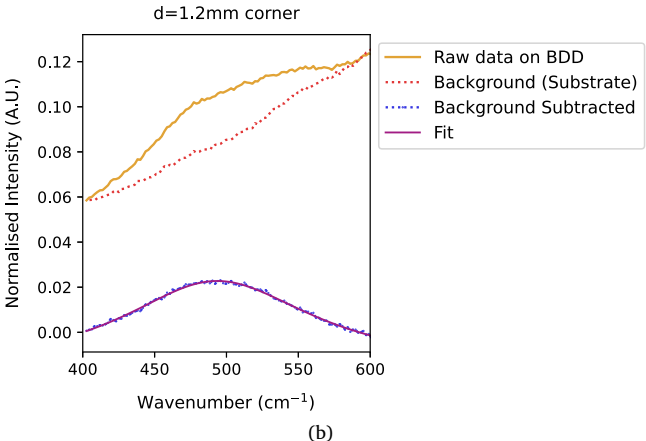


**Fig. 6.** (a) Full Raman spectrum on sample grown on d=1.2 mm, and on a diamond substrate. The signal for the data on BDD are mostly from the substrate layer due to the thin layer. (b) The raw data is normalised, subtracted by the background, and fitted using Fano lineshape.

A Raman spectrum is taken at the centre of each sample grown at different d, as a non-destructive measure of boron concentration [34, 35]. Raman was performed on all of the samples, which is a supplement to the SIMS measurements. Despite high absorption in the boron-doped layer, the Raman spectrum includes a dominant contribution from the diamond bulk within the micrometre-scale sampling depth of the microscope, as shown in Fig. 6a. The signal from the boron-doped layer is obtained by subtracting the background signal from the substrate, as shown in Fig. 6(b). The Raman spectrum shows a peak at around  $500 \, \mathrm{cm}^{-1}$  which is attributed to the incorporation of boron [35,36], and red-shifts with boron concentration using the equation from Ref. [35]

$$[B](cm^{-3}) = -6.99 \times 10^{19} (cm^{-2}) \times W (cm^{-1})$$

$$+ 3.57 \times 10^{22} (cm^{-3})$$
(9)

where W denotes the position of the  $500~\rm cm^{-1}$  when fitted with a Fano lineshape. Such a fitting has been performed on the peaks we obtained. A few examples of the fit are shown in Fig. 7, and the peak position and the corresponding boron concentration are shown in Fig. 7(b). For  $d=1.2~\rm mm$ , the calculated boron concentration  $\sim 1.4\times 10^{21}~\rm cm^{-3}$  agrees with the SIMS measurement at crater number 2–6 of the sample which is  $\sim 1.5\times 10^{21}~\rm cm^{-3}$ . For d ranging from 0.3 mm to 1.5 mm, the boron concentration does not appear to change significantly at  $[B] \sim 10^{21}~\rm cm^{-3}$ , with measured values within  $\sim 10\%$ . For  $d \geq 1.8~\rm mm$ , the boron concentration decreases to  $\sim 10^{20}~\rm cm^{-3}$ . Note that for  $d=0~\rm mm$ , the boron concentration is also on the order of  $\sim 10^{20}~\rm cm^{-3}$ ,

which is one order of magnitude lower than the samples grown at 0.3 mm  $\leq d \leq$  1.5 mm. The simulation predicts a significant change in plasma parameters as d increases, but the experimental result does not show significant variation for 0.3 mm  $\leq d \leq$  1.5 mm.

We performed Raman spectroscopy at the corners of a few samples, as shown in Fig. 7(b), to compare with the boron concentration at the centre of the sample. The boron concentration near the corner of those samples is, in general, higher than that in the centre, which agrees with our previous SIMS and critical temperature measurements, as well as the COMSOL simulation. Note that for d=0.0 mm,  $[B]\sim 10^{20}$  cm<sup>-3</sup> near the centre, but near the corner the boron concentration is one order of magnitude higher. This is different from the other two data points collected from the corner of the samples grown with d=0.3 mm and d=1.2 mm, which  $[B]\sim 10^{21}$  cm<sup>-3</sup> both near the centre and corner of the sample.

For comparison, the growth rate of the samples is measured and shown in Fig. 8. For  $0.0~\mathrm{mm} \leq d \leq 1.8~\mathrm{mm}$ , the sample shows a growth rate plateau; for  $1.8~\mathrm{mm} \leq d \leq 2.1~\mathrm{mm}$ , the growth rate decreases. This is not consistent with the simulations and understanding of growth chemistry, where the hydrogen number density determines the diamond growth rate; and is not consistent with previous reports of growth rate in recess holders [20]. In the COMSOL simulation, the hydrogen number density decreases with increasing d, suggesting the growth rate should increase as d increases; but the growth rate diverges from this trend: in the experiment, the growth rate does not change much in the range of  $0.0~\mathrm{mm} \leq d \leq 1.8~\mathrm{mm}$ . This, along with the Raman results, will be discussed further in Section 5.2.

#### 5. Discussion

## 5.1. Effects of the faraday cage on doping uniformity

Efforts have been made to achieve heavy boron doping in our local metallic cylindrical CVD reactor under various growth conditions; however, non-uniform boron doping across the substrate has been a significant problem without the use of a Faraday cage. Growth on pedestal-type sample holders results in strong boron incorporation anisotropy, with higher concentrations near the sample edges; and light doping in the centre, making the substrate unsuitable for superconducting devices (results not shown). In a cylindrical CVD reactor, the metallic sample holder forms part of the PEC boundary condition of the model, limiting the ability to adjust the sample-to-plasma distance.

In contrast, we have found that the addition of a Faraday cage pins the plasma down at the desired position at the bottom of the cavity, with the top of the cage serves as part of the boundary conditions. The Faraday cage suppresses the intensity of the E-field inside the cage, but still allows a significant E-field to exist at the sample surface, which suggests plasma is not completely excluded from the inside of the cage. Near the sample edge, the Faraday cage results in a reduced enhancement of the local E-field, because the intense E-field is now focused on the top of the cage. This leads to a more uniform E-field spatial distribution and, consequently, a more uniform boron doping level across the entire sample.

In the case of d=0.0 mm, the boron concentration near the corner and centre of the sample differs by an order of magnitude. In this case, the surface of the sample is at the same height as the top of the cage, allowing the plasma to cling to both the edges of the sample and the top of the cage. Yamada et al. [37] show a similar effect with a recess-type sample holder. The ratio between different gas species near the corners is presumably different from the centre, because of the enhanced local microwave plasma density near the edges, and therefore result in higher boron concentration near the edges than the centre of the sample. Therefore, the use of a cage enhances the uniformity of plasma parameters, the doping uniformity of boron, as demonstrated experimentally and suggested through simulation.

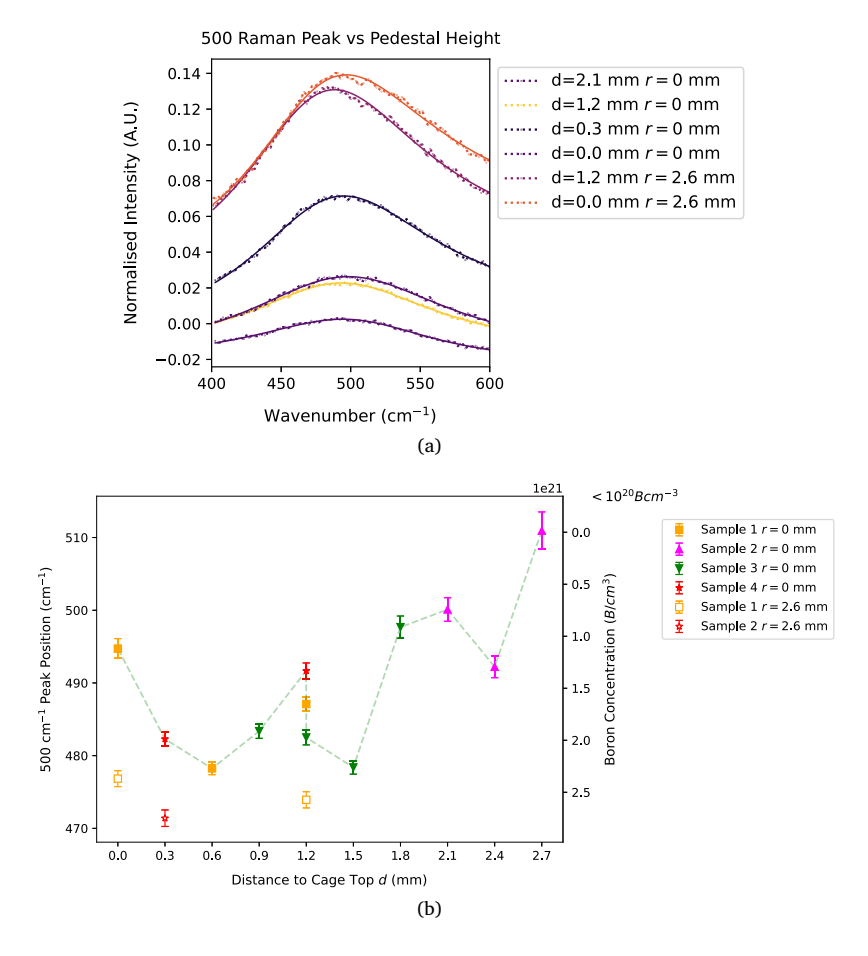
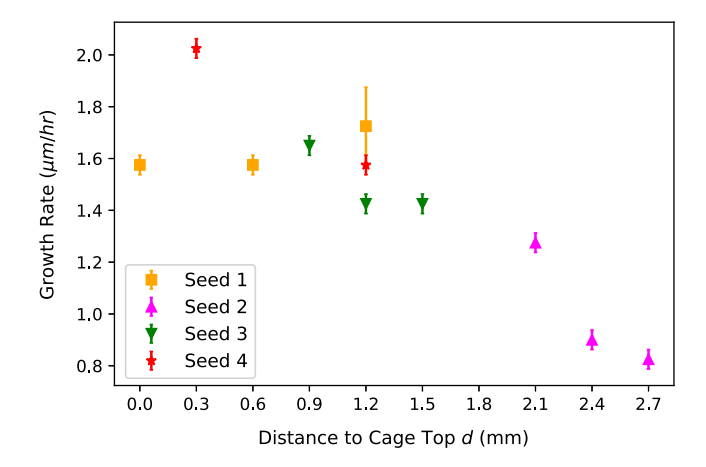


Fig. 7. (a) A few examples of the Fano fit. (b) Raman peak position with respect to d. Notice that the zero and negative value in the y-axis on the right hand side shows the "zero" point of the boron concentration conversion equation, which corresponds to a low boron concentration of  $n_B \sim 10^{19}$  cm<sup>-3</sup>.



**Fig. 8.** Growth rate as a function of distance to the cage top, d. The growth rate is similar for samples ranging from d=1.5 mm to d=0.0 mm, and decreases for samples with  $d\geq 2.1$  mm. To reduce the effect of substrate misorientation angle on doping concentration, the samples are cut into pieces of  $2\times 2$  mm, and processed individually. The pieces coming from the same original seed are labelled as "Seed 1–4".

#### 5.2. Position of the sample inside the plasma

In a NIRIM-type CVD reactor, the plasma can be ignited at the intersection of the waveguide and quartz tube, independent of the sample. Therefore, the position of the sample holder can be isolated

from the position of the plasma, allowing for better control over the growth conditions through the sample's position. Prawer et al. [21] showed that the position of the sample inside the plasma ball affects the crystalline quality of diamond; as well as the example mentioned earlier [22] that the boron doping efficiency in the solid phase can be controlled by changing the sample position in the plasma. In both examples, the activated gas species are presumably different as the sample position with respect to the plasma changes. For example, Silva et al. [24] show that the methyl species CH3, which diffuse on the substrate surface and react to form a C-C bond that is essential for diamond growth [38], have a spatial variation in both r- and zcoordinates. For boron doping, the main species that is responsible for boron insertion is controversial. Studies have suggested both BH and B species [39-41] are responsible for the insertion of boron into the surface C-C bond. Studies have also suggested the ratio between BH and CH<sub>3</sub> determines the doping efficiency [22,42].

As discussed in the previous subsection, the Faraday cage enables isolation of the sample position from the plasma, allowing control over the distance between the sample surface and the plasma. This can be achieved by designing pedestals of varying heights where the sample is placed. In this work, the cage is modelled as a tall cylinder surrounding a pedestal, rather than a cubic frame outside the pedestal. This geometry enables us to complete the numerical simulation effectively. However, for the doping efficiency and growth rate in the range  $0.0~\text{mm} \leq d \leq 1.8~\text{mm}$ , this simulation does not agree with the experimental results as shown in Figs. 8 and 7(b). Instead, the geometry is very similar to a recess holder. The consistency between the simulation and experimental results with a recess holder is within

expectation, where the growth rate decreases with increasing depth of the recess.

The discrepancies between the simulation and experimental results in our work suggest that the wire-frame aspects of the Faraday cage introduce additional complexity to the system. We found that the growth rate decay in the cage is ~ 33% over 2.8 mm of recess depth, where in a recess-type sample holder, the growth rate can decay for up to  $\sim 80\%$  [20] over a range of 2.0 mm recess depth. One of the differences between the cage and the enclosed/pocket recess-type holder, is that the cage has open windows on the sides. This special sample holder geometry may alter the flux and spatial distribution of the species near the sample surface, which could change the growth rate and doping efficiency behaviour as d increases. Further modelling to increase our understanding of how the Faraday cage changes the doping efficiency and growth rate in terms of d would need to include a H<sub>2</sub>/CH<sub>4</sub>/TMB plasma that details the spatial variation of H, CH<sub>4</sub> and BH or B species, and a more accurate physical representation of the real Faraday cage in 3-dimensions, which is computationally expensive and is therefore beyond the scope of this project. It is also possible that more complex fluid dynamics are involved in reactive species transport, which would require a more sophisticated computational approach.

Literature suggests that the boron source TMB is decomposed into species such as  $\mathrm{B(CH_3)}_x$  where x=0–3, and  $\mathrm{BH}^*$  upon dehydrogenation [43]. With the addition of higher TMB flow rate, Fiori et al. [42] observed that  $\mathrm{BH}^*$  emission signal increases in optical emission spectroscopy measurement; the produced  $\mathrm{BH}^*$  species interact with  $\mathrm{CH_3}$  near the substrate surface for growth. Furthermore, it is known that  $\mathrm{CH_3}$  concentration is higher near the plasma periphery. It can be seen from Ma et al. [44], that near the plasma periphery, both the B and BH to  $\mathrm{CH_3}$  ratios decrease, the  $\mathrm{CH_3}$  to H ratio increases, and the B and BH to H ratios decrease. Fiori et al. [42] have reported that the ratio between BH to  $\mathrm{CH_3}$  affects whether the process results in growth or etching of the sample.

In our case, as the sample surface moves further away from the plasma in the range of  $d \ge 1.8$  mm, the doping efficiency and growth decrease, which agrees with the simulation result reported by Ma et al. This suggests that moderately high B/C or B/H, and a relatively low CH<sub>3</sub>/H ratio is needed for heavy boron doping. Furthermore, the sample should be at a moderate distance from the hot plasma region: if d is too big or too small, the boron doping efficiency decreases. Using a Faraday cage to hold the hot plasma region away from the sample results in high doping efficiency without an apparent loss or tradeoff in growth rate, compared to immediate contact between the hot plasma and the sample when using a pedestal-type sample holder. This agrees with the result from Fiori [22], where they observed that doping efficiency is higher when the sample is further away (1 cm) from the hot plasma region. The actual distance between the plasma and sample surface differs in Fiori's and our work, which may be attributed to the differences in reactor and sample holder geometries.

The doping efficiency for  $d=1.2~\mathrm{mm}$  and  $d=0.0~\mathrm{mm}$  at the sample corner and centre is compared in Fig. 7(b). The doping efficiency is higher near the sample corner due to the more intense plasma. However, there is a trade-off between high uniformity and boron doping as mentioned in Section 4. The boron doping can be depleted near the sample centre, while boron doping near the corners and edges is enhanced at  $d=0.0~\mathrm{mm}$ . Therefore, one should choose a d value based on the balance between boron-doping efficiency, uniformity and growth rate.

# 6. Conclusion

In this work, we demonstrate that incorporating a Faraday cage as a sample holder within a cylindrical resonant cavity chamber enables the growth of uniformly doped superconducting diamond films. We obtained boron concentration of  $10^{21}~\rm cm^{-3}$  as shown by SIMS and Raman spectroscopy, with the bulk critical temperature reaching 1.3 K.

For optimal doping uniformity, the edge effect that enhances the local electric field should be reduced as much as possible.

The distance d between the plasma and the sample surface is important for controlling doping efficiency and growth rate. For  $d \geq 1.8$  mm, the doping efficiency and growth rate decrease as d increases. We observe a broad range of d values that produce similar growth rates and boron concentrations. This, along with the simulation, illustrates the differences between the recess-type sample holders and the Faraday cage.

The present work demonstrates the feasibility of the growth of heavily boron-doped diamond in a metallic cylindrical CVD reactor, and enhances our understanding of optimal growth conditions. This opens the possibility of making planar devices distributed spatially across the whole substrate where high uniformity of the superconducting properties is desired, for example microwave resonators or large arrays of superconducting nanowire single photon detectors.

#### CRediT authorship contribution statement

Y. Jiang: Writing – original draft, Visualization, Software, Methodology, Investigation, Formal analysis, Data curation. M. Bose: Writing – review & editing, Investigation. J.A. Cuenca: Writing – review & editing, Validation, Methodology. D.L. Creedon: Writing – review & editing, Methodology, Investigation, Conceptualization. J. Belcourt: Methodology. C.D. van Engers: Writing – review & editing, Investigation. A. Nadarajah: Methodology. K. Ganesan: Methodology. J.C. McCallum: Supervision. K. Fox: Writing – review & editing, Supervision. S. Prawer: Writing – review & editing, Supervision, Project administration, Funding acquisition. A. Stacey: Writing – review & editing, Validation, Supervision, Resources, Project administration, Methodology, Investigation, Funding acquisition, Conceptualization.

#### **Declaration of competing interest**

The authors declare the following financial interests/personal relationships which may be considered as potential competing interests: Yi Jiang reports administrative support was provided by University of New South Wales Australian Research Council Centre for Quantum Computation and Communication Technology. David N. Jamieson, Jeffrey C. McCallum reports administrative support was provided by University of New South Wales Australian Research Council Centre for Quantum Computation and Communication Technology. The corresponding author Yi Jiang has presented progress reports on this project that forms part of her PhD thesis at international conferences. If there are other authors, they declare that they have no known competing financial interests or personal relationships that could have appeared to influence the work reported in this paper.

# Acknowledgements

We acknowledge the Australian Research Council Discovery grants DP190102852 and DP150102703 for supporting this work. M. Bose is supported in part by Australian Research Council grants (DP200103233 and CE170100012). This work was performed in part at the Melbourne Centre for Nanofabrication (MCN) in the Victorian Node of the Australian National Fabrication Facility (ANFF). The exact parameters of the CVD reactor are provided by Cornes Technology and SEKI Diamond Systems.

# Data availability

Data will be shared on request, but the data for the geometry of the CVD reactor will remain confidential as requested by the manufacturer.

#### References

- [1] T. Kageura, M. Hideko, I. Tsuyuzaki, S. Amano, A. Morishita, T. Yamaguchi, Y. Takano, H. Kawarada, Superconductivity in nano- and micro-patterned high quality single crystalline boron-doped diamond films, Diam. Relat. Mater. 90 (2018) 181–187, http://dx.doi.org/10.1016/j.diamond.2018.10.013.
- [2] J.A. Cuenca, S. Mandal, J. Stritt, X. Zheng, J. Pomeroy, M. Kuball, A. Porch, O.A. Williams, Dielectric properties of diamond using an X-band microwave split dielectric resonator, Carbon 221 (2024) 118860, http://dx.doi.org/10.1016/ i.carbon.2024.118860.
- [3] S. Mandal, T. Bautze, O.A. Williams, C. Naud, E. Bustarret, F. Omnes, P. Rodiere, T. Meunier, C. Bauerle, L. Saminadayar, The diamond superconducting quantum interference device, ACS Nano 5 (9) (2011) 7144–7148, http://dx.doi.org/10. 1021/nn2018396.
- [4] T. Kageura, M. Hideko, I. Tsuyuzaki, A. Morishita, A. Kawano, Y. Sasama, T. Yamaguchi, Y. Takano, M. Tachiki, S. Ooi, K. Hirata, S. Arisawa, H. Kawarada, Single-crystalline boron-doped diamond superconducting quantum interference devices with regrowth-induced step edge structure, Sci. Rep. 9 (1) (2019) 15214, http://dx.doi.org/10.1038/s41598-019-51596-w.
- [5] M. Bose, D.L. Creedon, A. Barlow, M. Stuiber, G.M. Klemencic, S. Mandal, O. Williams, G. van Riessen, C.I. Pakes, Low-noise diamond-based D.C. Nano-SQUIDs, ACS Appl. Electron. Mater. 4 (5) (2022) 2246–2252, http://dx.doi.org/ 10.1021/acsaelm.2c00048.
- [6] M. Watanabe, A. Kawano, S. Kitagoh, T. Yamaguchi, Y. Takano, H. Kawarada, Stacked SNS josephson junction of all boron doped diamond, Phys. C-Supercond. Appl. 470 (2010) S613–S615, http://dx.doi.org/10.1016/j.physc.2009.11.061.
- [7] T. Bautze, S. Mandal, O.A. Williams, P. Rodière, T. Meunier, C. Bäuerle, Super-conducting nano-mechanical diamond resonators, Carbon 72 (2014) 100–105, http://dx.doi.org/10.1016/j.carbon.2014.01.060.
- [8] E.A. Ekimov, V.A. Sidorov, E.D. Bauer, N.N. Mel'nik, N.J. Curro, J.D. Thompson, S.M. Stishov, Superconductivity in diamond, Nature 428 (6982) (2004) 542–545, http://dx.doi.org/10.1038/nature02449.
- [9] Y. Takano, M. Nagao, I. Sakaguchi, M. Tachiki, T. Hatano, K. Kobayashi, H. Umezawa, H. Kawarada, Superconductivity in diamond thin films well above liquid helium temperature, Appl. Phys. Lett. 85 (14) (2004) 2851–2853, http://dx.doi.org/10.1063/1.1802389.
- [10] T. Klein, P. Achatz, J. Kacmarcik, C. Marcenat, F. Gustafsson, J. Marcus, E. Bustarret, J. Pernot, F. Omnes, B.E. Sernelius, C. Persson, A.F. da Silva, C. Cytermann, Metal-insulator transition and superconductivity in boron-doped diamond, Phys. Rev. B 75 (16) (2007) 7, http://dx.doi.org/10.1103/PhysRevB. 75.165313
- [11] Y. Takano, T. Takenouchi, S. Ishii, S. Ueda, T. Okutsu, I. Sakaguchi, H. Umezawa, H. Kawarada, M. Tachiki, Superconducting properties of homoepitaxial CVD diamond, Diam. Relat. Mater. 16 (4–7) (2007) 911–914, http://dx.doi.org/10. 1016/j.diamond.2007.01.027.
- [12] V. Mortet, A. Taylor, M. Davydova, J. Jiráek, L. Fekete, L. Klimsa, D. Simek, N. Lambert, S. Sedlakavo, J. Kopecek, P. Hazdra, Effect of substrate crystalline orientation on boron-doped homoepitaxial diamond growth, Diam. Relat. Mater. 122 (2022) http://dx.doi.org/10.1016/j.djamond.2022.108887.
- [13] H. Okazaki, T. Wakita, T. Muro, T. Nakamura, Y. Muraoka, T. Yokoya, S.I. Kurihara, H. Kawarada, T. Oguchi, Y. Takano, Signature of high T(c) above 25 K in high quality superconducting diamond, Appl. Phys. Lett. 106 (5) (2015) 052601, http://dx.doi.org/10.1063/1.4907411.
- [14] M. Kamo, Y. Sato, S. Matsumoto, N. Setaka, Diamond synthesis from gas phase in microwave plasma, J. Cryst. Growth 62 (3) (1983) 642–644, http://dx.doi. org/10.1016/0022-0248(83)90411-6.
- [15] J. Weng, F. Liu, L.W. Xiong, J.H. Wang, Q. Sun, Deposition of large area uniform diamond films by microwave plasma CVD, Vacuum 147 (2018) 134–142, http://dx.doi.org/10.1016/j.vacuum.2017.10.026.
- [16] A. Rifai, D. Creedon, N. Tran, M. Hejazi, D. Garrett, A.D. Greentree, E. Pirogova, A. Stacey, K. Fox, Highly uniform polycrystalline diamond coatings of threedimensional structures, Surf. Coat. Technol. 408 (2021) 126815, http://dx.doi. org/10.1016/j.surfcoat.2020.126815.
- [17] Z.L. Yang, Y.C. Liu, Z.J. Guo, J.J. Wei, J.L. Liu, L.X. Chen, C.M. Li, Deposition of uniform diamond films on three dimensional Si spheres by using faraday cage in MPCVD reactor, Diam. Relat. Mater. 142 (2024) 110767, http://dx.doi.org/ 10.1016/j.diamond.2023.110767.
- [18] S. Nad, Y.J. Gu, J. Asmussen, Growth strategies for large and high quality single crystal diamond substrates, Diam. Relat. Mater. 60 (2015) 26–34, http: //dx.doi.org/10.1016/j.diamond.2015.09.018.
- [19] M. Feng, P. Jin, X. Meng, P. Xu, J. Wu, Z. Wang, One-step growth of a nearly 2 mm thick CVD single crystal diamond with an enlarged surface by optimizing the substrate holder structure, J. Cryst. Growth 603 (2023) 127011, http://dx.doi.org/10.1016/j.jcrysgro.2022.127011.

- [20] G. Wu, M.H. Chen, J. Liao, The influence of recess depth and crystallographic orientation of seed sides on homoepitaxial growth of CVD single crystal diamonds, Diam. Relat. Mater. 65 (2016) 144–151, http://dx.doi.org/10.1016/j.diamond. 2016.03.011.
- [21] S. Prawer, A. Hoffman, S.A. Stuart, R. Manory, P. Weiser, C.S. Lim, J.M. Long, F. Ninio, Correlation between crystalline perfection and film purity for chemically vapor-deposited diamond thin-films grown on fused quartz substrates, J. Appl. Phys. 69 (9) (1991) 6625–6631, http://dx.doi.org/10.1063/1.348876.
- [22] A. Fiori, Nouvelles Générations de Structures en Diamant Dopé au Bore par Technique de Delta-Dopage Pour L'électronique de Puissance: Croissance Par CVD et Caractérisation (Ph.D. thesis), 2012.
- [23] W. Xu, S. Sun, J. Elambasseril, Q. Liu, M. Brandt, M. Qian, Ti-6Al-4V additively manufactured by selective laser melting with superior mechanical properties, JOM 67 (3) (2015) 668-673, http://dx.doi.org/10.1007/s11837-015-1297-8.
- [24] F. Silva, K. Hassouni, X. Bonnin, A. Gicquel, Microwave engineering of plasmaassisted CVD reactors for diamond deposition, J. Phys.: Condens. Matter. 21 (36) (2009) 364202, http://dx.doi.org/10.1088/0953-8984/21/36/364202.
- [25] M. Füner, C. Wild, P. Koidl, Numerical simulations of microwave plasma reactors for diamond CVD, Surf. Coat. Technol. 74–75 (1995) 221–226, http://dx.doi.org/ 10.1016/0257-8972(95)08232-8.
- [26] G. Shivkumar, S.S. Tholeti, M.A. Alrefae, T.S. Fisher, A.A. Alexeenko, Analysis of hydrogen plasma in a microwave plasma chemical vapor deposition reactor, J. Appl. Phys. 119 (11) (2016) 113301, http://dx.doi.org/10.1063/1.4943025.
- [27] D.G. Goodwin, Scaling laws for diamond chemical-vapor deposition. II. atomic hydrogen transport, J. Appl. Phys. 74 (11) (1993) 6895–6906, http://dx.doi.org/ 10.1063/1.355064.
- [28] J.A. Cuenca, S. Mandal, E.L.H. Thomas, O.A. Williams, Microwave plasma modelling in clamshell chemical vapour deposition diamond reactors, Diam. Relat. Mater. 124 (2022) 108917, http://dx.doi.org/10.1016/j.diamond.2022. 108917.
- [29] W. Tan, T.A. Grotjohn, Modelling the electromagnetic field and plasma discharge in a microwave plasma diamond deposition reactor, Diam. Relat. Mater. 4 (9) (1995) 1145–1154, http://dx.doi.org/10.1016/0925-9635(95)00291-X.
- [30] H. Yamada, Numerical simulations to study growth of single-crystal diamond by using microwave plasma chemical vapor deposition with reactive (H, C, N) species, Japan. J. Appl. Phys. 51 (9R) (2012) 090105, http://dx.doi.org/10.1143/ JJAP.51.090105.
- [31] J. Achard, F. Silva, A. Tallaire, X. Bonnin, G. Lombardi, K. Hassouni, A. Gicquel, High quality MPACVD diamond single crystal growth: High microwave power density regime, J. Phys. D: Appl. Phys. 40 (20) (2007) 6175–6188, http://dx.doi.org/10.1088/0022-3727/40/20/S04.
- [32] R.J. Zhang, S.T. Lee, Y.W. Lam, Characterization of heavily boron-doped diamond films, Diam. Relat. Mater. 5 (11) (1996) 1288–1294, http://dx.doi.org/10.1016/ 0925-9635(96)00539-0.
- [33] X. Blase, E. Bustarret, C. Chapelier, T. Klein, C. Marcenat, Superconducting group-IV semiconductors, Nature Mater. 8 (5) (2009) 375–382, http://dx.doi. org/10.1038/nmat2425.
- [34] M. Werner, O. Dorsch, H.U. Baerwind, E. Obermeier, L. Haase, W. Seifert, A. Ringhandt, C. Johnston, S. Romani, H. Bishop, P.R. Chalker, Charge-transport in heavily B-doped polycrystalline diamond films, Appl. Phys. Lett. 64 (5) (1994) 595–597, http://dx.doi.org/10.1063/1.111088.
- [35] V. Mortet, Z.V. Zivcová, A. Taylor, O. Frank, P. Hubík, D. Trémouilles, F. Jomard, J. Barjon, L. Kavan, Insight into boron-doped diamond Raman spectra characteristic features, Carbon 115 (2017) 279–284, http://dx.doi.org/10.1016/j.carbon.2017.01.022.
- [36] M. Bernard, C. Baron, A. Deneuville, About the origin of the low wave number structures of the Raman spectra of heavily boron doped diamond films, Diam. Relat. Mater. 13 (4–8) (2004) 896–899, http://dx.doi.org/10.1016/j.diamond. 2003.11.082.
- [37] H. Yamada, A. Chayahara, Y. Mokuno, Y. Horino, S. Shikata, Simulation of microwave plasmas concentrated on the top surface of a diamond substrate with finite thickness, Diam. Relat. Mater. 15 (9) (2006) 1383–1388, http://dx.doi. org/10.1016/j.diamond.2005.10.018.
- [38] A. Gicquel, K. Hassouni, F. Silva, J. Achard, CVD diamond films: From growth to applications, Curr. Appl. Phys. 1 (6) (2001) 479–496, http://dx.doi.org/10. 1016/S1567-1739(01)00061-X.
- [39] Q. Liang, J.G. Harrison, Y.K. Vohra, Modeling of nitrogen/diborane/methane/hy-drogen plasma for nanocrystalline diamond growth: Comparison with experimental data, Diam. Relat. Mater. 17 (12) (2008) 2067–2070, http://dx.doi.org/10.1016/j.diamond.2008.07.001.
- [40] A. Cheesman, J.N. Harvey, M.N.R. Ashfold, Computational studies of elementary steps relating to boron doping during diamond chemical vapour deposition, Phys. Chem. Phys. 7 (6) (2005) 1121–1126, http://dx.doi.org/10.1039/ B418664H.

- [41] J. Ma, J.C. Richley, D.R.W. Davies, A. Cheesman, M.N.R. Ashfold, Y.A. Mankelevich, Spectroscopic and modeling investigations of the gas-phase chemistry and composition in microwave plasma activated B2H6/Ar/H2 mixtures, J. Phys. Chem. A 114 (7) (2010) 2447–2463, http://dx.doi.org/10.1021/jp9094694.
- [42] A. Fiori, T. Teraji, Plasma etching phenomena in heavily boron-doped diamond growth, Diam. Relat. Mater. 76 (2017) 38–43, http://dx.doi.org/10.1016/j. diamond.2017.04.007.
- [43] M. Imam, C. Höglund, J. Jensen, S. Schmidt, I.G. Ivanov, R. Hall-Wilton, J. Birch, H. Pedersen, Trimethylboron as single-source precursor for boron–carbon thin film synthesis by plasma chemical vapor deposition, J. Phys. Chem. C 120 (38) (2016) 21990–21997, http://dx.doi.org/10.1021/acs.jpcc.6b06529.
- [44] J. Ma, J.C. Richley, D.R.W. Davies, M.N.R. Ashfold, Y.A. Mankelevich, Spectro-scopic and modeling investigations of the gas phase chemistry and composition in microwave plasma activated B2H6/CH4/Ar/H2 mixtures, J. Phys. Chem. A 114 (37) (2010) 10076–10089, http://dx.doi.org/10.1021/jp104532y.